

## Elastic wavefield separation based on the Helmholtz decomposition

Hejun Zhu<sup>1</sup>

### ABSTRACT

Divergence and curl operators used for the decomposition of P- and S-wave modes in elastic reverse time migration (RTM) change the amplitudes, units, and phases of extrapolated wavefields. I separate the P- and S-waves in elastic media based on the Helmholtz decomposition. The decomposed wavefields based on this approach have the same amplitudes, units, and phases as the extrapolated wavefields. To avoid expensive multidimensional integrals in the Helmholtz decomposition, I introduce a fast Poisson solver to efficiently solve the vector Poisson's equation. This fast algorithm allows us to reduce computational complexity from  $O(N^2)$  to  $O(N \log N)$ , where  $N$  is the total number of grid points. Because the decomposed P- and S-waves are vector fields, I use vector imaging conditions to construct PP-, PS-, SS-, and SP-images. Several 2D numerical examples demonstrate that this approach allows us to accurately and efficiently decompose P- and S-waves in elastic media. In addition, elastic RTM images based on the vector imaging conditions have better quality and avoid polarity reversal in comparison with images based on the divergence and curl separation or direct component-by-component crosscorrelation.

### INTRODUCTION

Traditional seismic migration techniques approximate the subsurface as acoustic and only consider compressional energies. Although this approximation is useful and efficient in practice, it ignores the importance of S-waves and might introduce artifacts into migration images. For instance, for large incident angles, S-waves may have larger amplitudes in comparison with P-waves and provide us important constraints about material properties in the subsurface. Furthermore, simultaneously analyzing multi-

component migration images, such as PP, PS, SS, and SP, enables us to better interpret imaging results and locate reservoirs.

Migration techniques can be classified as either based on ray approximation, such as Kirchhoff (Schneider, 1978; Bleistein, 1987) and beam migration (Hill, 1990, 2001), or wave-equation-based approaches, such as reverse time migration (RTM) (Baysal et al., 1983; McMechan, 1983; Whitmore, 1983) and one-way migration (Claerbout, 1971; Zhang et al., 2003). To date, synthetic and field experiments have shown that RTM has better performance in imaging complex structures in comparison with other migration techniques. In this study, I focus on RTM in elastic media.

One way for elastic RTM is to directly extrapolate source and receiver wavefields into the subsurface by solving the elastic-wave equation. Then, the horizontal (H) and vertical (V) component wavefields are used to construct VV-, VH-, HH-, and HV-images (Chang and McMechan, 1987). Because the horizontal and vertical component wavefields may involve P- and S-waves, this approach might introduce crosstalk artifacts into the migration results. For instance, VV component images not only represent PP-reflectivity, but also include PS, SS, and SP information. Another way to perform elastic RTM is to decompose recorded seismograms into their P- and S-components. Then, acoustic-wave equations with P- and S-velocities are used to extrapolate scalar wavefields and build images.

A better way to perform elastic RTM is based on wave-mode decomposition. In this category, the first step is to extrapolate the source and receiver waves into the subsurface using acquired multicomponent data as boundary conditions. Then, some wave-mode decomposition approaches are used to separate the P- and S-waves. Finally, imaging conditions are applied to build direct (PP, SS) and converted (PS, SP) images by crosscorrelating the P- and S-components of the extrapolated wavefields. For instance, divergence and curl operators have been used to decompose extrapolated wavefields into scalar and vector potentials, which are then used to construct multicomponent images (Sun and McMechan, 2001; Sun et al., 2006; Yan and Sava, 2008). However, as noticed by Sun et al. (2001), the decomposed scalar and vector potentials do not have the correct amplitudes and units. The summa-

Manuscript received by the Editor 4 August 2016; revised manuscript received 27 October 2016; published online 16 February 2017.

<sup>1</sup>The University of Texas at Dallas, Department of Geosciences, Richardson, Texas, USA. E-mail: hejun.zhu@utdallas.edu.  
© 2017 Society of Exploration Geophysicists. All rights reserved.

tion of these potentials cannot reproduce the input wavefields. In addition, the divergence and curl differential operators introduce phase shifts to the decomposed wavefields. Considering these limitations, Zhang and McMechan (2010) propose an approach to decompose the P- and S-vector fields in the wavenumber domains. Ma and Zhu (2003) and Wang and McMechan (2015) introduce a new stress field in the wave equation to accurately separate the P- and S-energies. Yan and Xie (2012) propose an angle-domain imaging condition for elastic RTM. Wang et al. (2016) introduce scalar and vector imaging conditions for isotropic and transversely isotropic media. Considering connections between RTM and gradients in full-waveform inversion, Zhu et al. (2009) propose a new elastic RTM imaging condition based on impedance kernels (Luo et al., 2009), which avoids “well-known,” low-frequency artifacts observed in most RTM images due to backscattering energies (Liu et al., 2011). Douma et al. (2010) show that this imaging condition is equivalent for the application of Laplace filtering during the post-processing of RTM.

The approach proposed in this paper is based on the direct application of the Helmholtz decomposition (Morse and Feshbach, 1953) to separate P- and S-wave modes. The advantages of the Helmholtz decomposition include the preservation of correct units, amplitudes, and phases. The difficulties of the Helmholtz decomposition are expensive operations for either calculating multidimensional integrals (Zhang and McMechan, 2010) or solving a vector Poisson’s equation. The computational complexity of calculating the multidimensional integral is  $O(N^2)$ , where  $N$  is the total number of grid points. This is impractical for 2D and 3D elastic RTM. In this paper, I introduce a fast Poisson’s solver (Strang, 2007) to efficiently solve the vector Poisson’s equation with computational complexity of  $O(N \log N)$ . With this fast algorithm, I am able to directly apply the Helmholtz decomposition in wave-mode separation. Because the P- and S-waves are decomposed into vector fields, I modify the classic scalar imaging condition to vector imaging conditions for constructing PP-, PS-, SS-, and SP-images.

This paper is organized as follows: First, I describe the Helmholtz decomposition for isolating P- and S-waves. Then, a fast Poisson’s solver is introduced to efficiently solve the vector Poisson’s equation in the Helmholtz decomposition. Next, vector imaging conditions are proposed to construct PP-, PS-, SS-, and SP-images. Finally, several 2D numerical examples are used to demonstrate that this approach enables us to accurately and efficiently separate the P- and S-energies as well as constructing high-quality elastic RTM images.

## METHODS

### The Helmholtz decomposition

The propagation of P- and S-waves in elastic, homogeneous, isotropic media can be described by the elastic-wave equation (Aki and Richards, 1980),

$$\rho \frac{\partial^2 \mathbf{u}}{\partial t^2} = \mathbf{f} + (\lambda + 2\mu) \nabla(\nabla \cdot \mathbf{u}) - \mu \nabla \times \nabla \times \mathbf{u}, \quad (1)$$

where  $\mathbf{u}$  is the displacement vector,  $\lambda$  and  $\mu$  are the Lamé coefficients,  $\rho$  is the density, and  $\mathbf{f}$  is the source term used to excite wavefields.

In elastic media, wavefield  $\mathbf{u}$  contains P-wave displacement  $\mathbf{u}^P$  and S-wave displacement  $\mathbf{u}^S$ . Based on the Helmholtz decomposition (Morse and Feshbach, 1953), wavefield  $\mathbf{u}$  can be decomposed into a scalar potential  $\phi$  and a vector potential  $\Psi$

$$\mathbf{u} = \mathbf{u}^P + \mathbf{u}^S = \nabla\phi + \nabla \times \Psi. \quad (2)$$

The relationship between the P/S-displacements and scalar/vector potentials can be expressed as follows:

$$\mathbf{u}^P = \nabla\phi, \quad \mathbf{u}^S = \nabla \times \Psi. \quad (3)$$

These fields have to satisfy the following requirements because P-waves are curl-free and S-waves are divergence-free

$$\nabla \times \mathbf{u}^P = 0, \quad \nabla \cdot \mathbf{u}^S = 0, \quad \nabla \cdot \Psi = 0. \quad (4)$$

Given a wavefield  $\mathbf{u}$ , to calculate the scalar and vector potentials, I introduce a new vector field  $\mathbf{w}$  that satisfies the following vector Poisson’s equation:

$$\nabla^2 \mathbf{w} = \mathbf{u}. \quad (5)$$

Furthermore, the Laplace operator  $\nabla^2$  can be decomposed into two terms

$$\nabla^2 \mathbf{w} = \nabla(\nabla \cdot \mathbf{w}) - \nabla \times \nabla \times \mathbf{w}. \quad (6)$$

Comparing equations 2, 5, and 6, I have the following relations between scalar/vector potentials and the new vector field  $\mathbf{w}$ :

$$\phi = \nabla \cdot \mathbf{w}, \quad \Psi = -\nabla \times \mathbf{w}. \quad (7)$$

Combined with equation 3, the P- and S-displacements can be expressed by the vector field  $\mathbf{w}$  as

$$\mathbf{u}^P = \nabla(\nabla \cdot \mathbf{w}), \quad \mathbf{u}^S = -\nabla \times \nabla \times \mathbf{w}. \quad (8)$$

Once I am able to efficiently solve the vector Poisson’s equation (equation 5), P- and S-wave displacements can be directly decomposed by equation 8.

### Analytical Green’s functions for the vector Poisson’s equation

The vector Poisson’s equation has analytical Green’s functions for 2D and 3D media. For instance, 2D Green’s function for equation 5 is

$$\mathbf{G}^{2D}(\mathbf{x}; \mathbf{x}_0) = \frac{\ln |\mathbf{x} - \mathbf{x}_0|}{2\pi}, \quad (9)$$

where  $\mathbf{G}^{2D}$  is the Green’s function for 2D vector Poisson’s equation;  $\mathbf{x}$  and  $\mathbf{x}_0$  are the locations of source and receiver, respectively.

Based on the representation theorem (Aki and Richards, 1980), I can rewrite the P/S separation scheme (equation 8) as follows:

$$\begin{aligned}\mathbf{u}^p(\mathbf{x}) &= \nabla \left( \nabla \cdot \iint \mathbf{u}(\mathbf{x}') \frac{\ln |\mathbf{x} - \mathbf{x}'|}{2\pi} d^2 \mathbf{x}' \right), \\ \mathbf{u}^s(\mathbf{x}) &= -\nabla \times \nabla \times \iint \mathbf{u}(\mathbf{x}') \frac{\ln |\mathbf{x} - \mathbf{x}'|}{2\pi} d^2 \mathbf{x}'.\end{aligned}\quad (10)$$

Similarly, Green's function  $\mathbf{G}^{3D}$  for the 3D vector Poisson's equation is

$$\mathbf{G}^{3D}(\mathbf{x}; \mathbf{x}_0) = -\frac{1}{4\pi|\mathbf{x} - \mathbf{x}_0|}.\quad (11)$$

Then, P- and S-wave displacements in 3D elastic media can be decomposed by

$$\begin{aligned}\mathbf{u}^p(\mathbf{x}) &= -\nabla \left( \nabla \cdot \iiint \frac{\mathbf{u}(\mathbf{x}')}{4\pi|\mathbf{x} - \mathbf{x}'|} d^3 \mathbf{x}' \right), \\ \mathbf{u}^s(\mathbf{x}) &= \nabla \times \nabla \times \iiint \frac{\mathbf{u}(\mathbf{x}')}{4\pi|\mathbf{x} - \mathbf{x}'|} d^3 \mathbf{x}'.\end{aligned}\quad (12)$$

Although equations 10 and 12 are well-known solutions (Morse and Feshbach, 1953), they are rarely used in the decomposition of P- and S-waves. To implement these equations, we have to perform the 2D or 3D integral for each grid point. The computational complexity of this multidimensional integral is  $O(N^2)$ , where  $N$  is the total number of grid points in the simulation domain. It is expensive for 2D problems and prohibitive for 3D models. In addition, in the 2D and 3D analytical Green's functions (equations 10 and 12), there are singularities when the distance equals zero, leading to numerical instability for the evaluation of  $1/|\mathbf{x} - \mathbf{x}'|$  and  $\ln |\mathbf{x} - \mathbf{x}'|$ . Thus, to separate P- and S-waves with the Helmholtz decomposition (equation 8), we need efficient solvers for the vector Poisson's equation (equation 5).

### Fast Poisson solver

By taking advantage of the fast Fourier transform (FFT), we are able to efficiently solve equation 5 by a fast Poisson's solver (Strang, 2007). First, I discretize the 2D scalar Poisson's equation using a five-point finite difference stencil

$$4w_{i,j} - w_{i-1,j} - w_{i+1,j} - w_{i,j-1} - w_{i,j+1} = -h^2 u_{i,j},\quad (13)$$

where I assume that the horizontal and vertical grid spacings are  $h$ . Because the vector Poisson's equation can be solved component-by-component, I only present the algorithm for a 2D scalar Poisson's equation. It can be easily extended to 3D cases.

I decompose  $w$  and  $u$  via the discrete sine transform as

$$\begin{aligned}w_{i,j} &= \sum_{k=1}^{N_x-1} \sum_{l=1}^{N_z-1} \hat{W}_{k,l} \sin \frac{ik\pi}{N_x} \sin \frac{jl\pi}{N_z}, \\ u_{i,j} &= \sum_{k=1}^{N_x-1} \sum_{l=1}^{N_z-1} \hat{U}_{k,l} \sin \frac{ik\pi}{N_x} \sin \frac{jl\pi}{N_z},\end{aligned}\quad (14)$$

where  $\hat{W}$  and  $\hat{U}$  are the Fourier components of  $w$  and  $u$ , respectively;  $N_x$  and  $N_z$  are the numbers of grid points in the horizontal and vertical directions, respectively.

Substituting the above discrete sine transforms into the discretized Poisson's equation (equation 13) and using trigonometric relations, I can obtain a relation between the Fourier components  $\hat{W}$  and  $\hat{U}$  as

$$\hat{W}_{k,l} = \hat{U}_{k,l}/\lambda_{k,l},\quad (15)$$

where  $\lambda_{k,l}$  is the eigenvalue of the discretized Laplace operator, which can be computed by

$$\lambda_{k,l} = 4 - 2 \cos \frac{k\pi}{N_x} - 2 \cos \frac{l\pi}{N_z}.\quad (16)$$

With this relation, the fast Poisson solver can be described by the following three steps:

- 1) We compute the Fourier components of wavefield  $u$  via the sine transform:

$$\hat{U}_{k,l} = \frac{1}{N_x N_z} \sum_{i=1}^{N_x-1} \sum_{j=1}^{N_z-1} u_{i,j} \sin \left( -\frac{ik\pi}{N_x} \right) \sin \left( -\frac{jl\pi}{N_z} \right).\quad (17)$$

- 2) We compute the Fourier component  $\hat{W}$  based on  $\hat{U}$  and the eigenvalues  $\lambda$ :

$$\hat{W}_{k,l} = \hat{U}_{k,l}/\lambda_{k,l}.\quad (18)$$

- 3) We combine the solution  $w$  based on its Fourier component  $\hat{W}$ :

$$w_{i,j} = \sum_{k=1}^{N_x-1} \sum_{l=1}^{N_z-1} \hat{W}_{k,l} \sin \frac{ik\pi}{N_x} \sin \frac{jl\pi}{N_z}.\quad (19)$$

The computation in equation 18 is negligible in comparison with sine transforms in equations 17 and 19. These transforms can be efficiently calculated based on the FFT. Therefore, the total computational complexity of the fast Poisson's solver is  $O(N \log N)$  in comparison to  $O(N^2)$  for the analytical solutions based on the Green's functions (equations 10 and 12). In this study, FFTW (Frigo and Johnson, 2017) is used to compute the discrete sine transforms.

### Vector imaging conditions in elastic RTM

Because the decomposed P and S are vector fields, I modify the scalar zero-lag crosscorrelation imaging condition into several vector imaging conditions to construct PP-, SS-, PS-, and SP-images

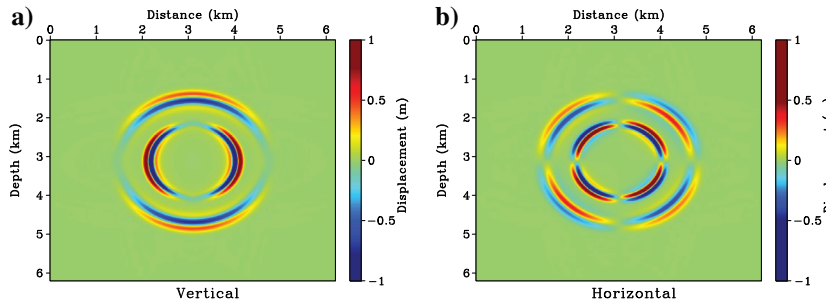


Figure 1. (a) The vertical and (b) horizontal component displacements in a homogeneous model, simulated by a finite-difference solver with a vertical force at (3 km, 3 km).

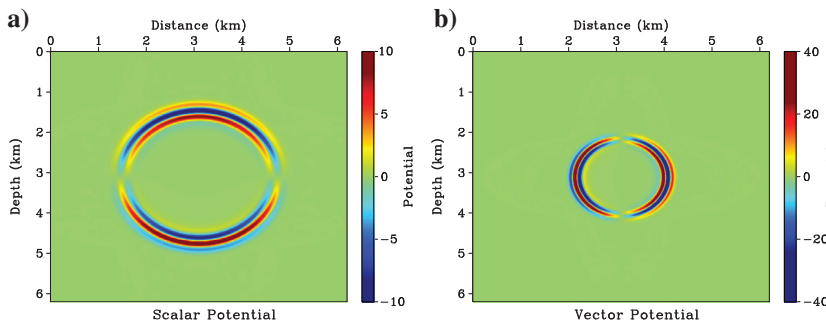


Figure 2. Decomposed (a) scalar and (b) vector potentials based on the divergence and curl operators.

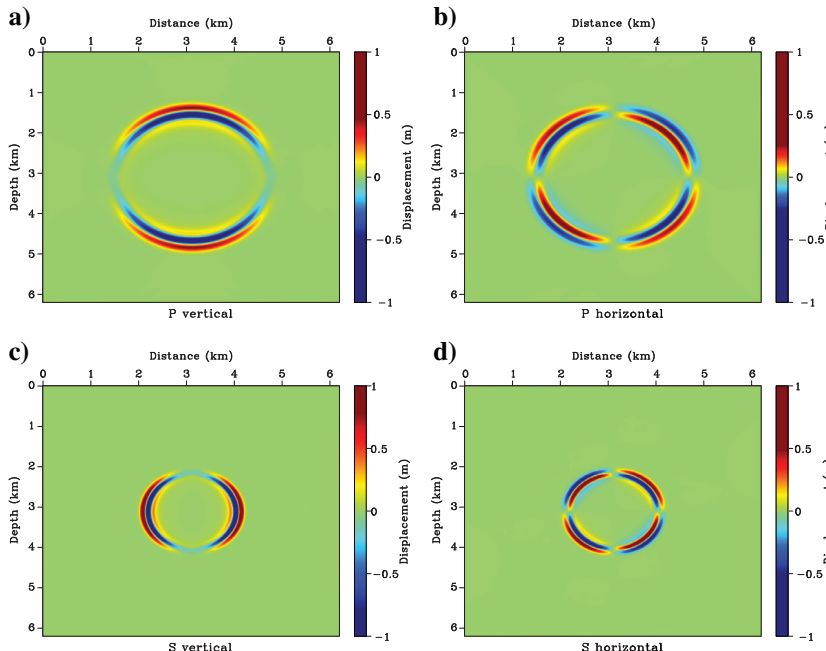


Figure 3. Isolated P- and S-wave displacements based on the Helmholtz decomposition. Panels (a and b) are the vertical and horizontal component P-wavefields. Panels (c and d) are the vertical and horizontal component S-wavefields.

$$\begin{aligned} I^{PP}(\mathbf{x}) &= \int \mathbf{u}_s^P(\mathbf{x}, t) \cdot \mathbf{u}_r^P(\mathbf{x}, t) dt, \\ I^{SS}(\mathbf{x}) &= \int \mathbf{u}_s^S(\mathbf{x}, t) \cdot \mathbf{u}_r^S(\mathbf{x}, t) dt, \\ I^{PS}(\mathbf{x}) &= \int \mathbf{u}_s^P(\mathbf{x}, t) \cdot \mathbf{u}_r^S(\mathbf{x}, t) dt, \\ I^{SP}(\mathbf{x}) &= \int \mathbf{u}_s^S(\mathbf{x}, t) \cdot \mathbf{u}_r^P(\mathbf{x}, t) dt, \end{aligned} \quad (20)$$

where  $I^{PP}$ ,  $I^{SS}$ ,  $I^{PS}$ , and  $I^{SP}$  are the images for PP-, SS-, PS-, and SP-reflectivities, respectively;  $\mathbf{u}_s$  and  $\mathbf{u}_r$  are the extrapolated source and receiver wavefields, respectively.

### Wave-mode decomposition based on divergence and curl operators

I use conventional divergence and curl operators as references to compare P/S decomposition results based on the Helmholtz decomposition. The P- and S-energies are decomposed based on the divergence and curl operators (Sun and McMechan, 2001; Sun et al., 2006; Yan and Sava, 2008):

$$P = \nabla \cdot \mathbf{u}, \quad \mathbf{S} = \nabla \times \mathbf{u}. \quad (21)$$

As pointed out by Sun et al. (2001) and Zhang and McMechan (2010), the decomposed wavefields based on equation 21 do not have correct physical meanings. The units of P- and S-energies are not displacements as the input wavefield  $\mathbf{u}$ . A more serious problem is that these differential operators introduce phase shifts to the decomposed wavefields. In addition, with these operations, P-wave energies are represented by a scalar field, which should be a vector field as the input wavefield.

### EXAMPLES

In the first example, I demonstrate P- and S-wave decomposition in a homogeneous model with  $V_P = 4 \text{ km/s}$ ,  $V_S = 2.35 \text{ km/s}$ , and  $\rho = 2.25 \text{ g/cm}^3$ . A forth-order staggered-grid finite-difference scheme (Virieux, 1984, 1986) is used to solve the 2D elastic-wave equation and simulate the propagation of P-SV waves. A vertical force at (3 km, 3 km) is used to excite the vertical and horizontal component wavefields as shown in Figure 1. A Ricker wavelet with a center frequency of 10 Hz is used in this experiment.

Based on the divergence and curl operators (equation 21), the separated scalar and vector potentials are illustrated in Figure 2. These potentials do not preserve the correct amplitudes, units, and phases as the input wavefields. In this 2D P-SV experiment, both potentials are scalar

fields. However, the P- and S-wave displacements should be vector fields involving the vertical and horizontal components.

Next, I decompose the input wavefield into P- and S-waves using the Helmholtz decomposition. The decomposed P- and S-waves are shown in Figure 3a–3d. Amplitudes, phases, and units of these wavefields are the same as the input. The P- and S-displacements are vector fields with the horizontal and vertical components. Therefore, I can directly sum the decomposed P- and S-waves to accurately reconstruct the input wavefield as illustrated in Figure 4a and 4b. In addition, I can compute differences between the input and reconstructed wavefields as shown in Figure 4c and 4d. Although there are some leakages of S-wave energies and numerical artifacts in the differences, their magnitudes are much smaller than the input wavefields (approximately 2%). There are some artifacts around the boundaries due to the Dirichlet boundary condition used in the fast Poisson's solver.

In the second example, I use the left portion of 2D Marmousi2 model as an example. The  $V_P$  model is shown in Figure 5a. The S-velocity is a scaled version of P-velocity with  $V_P/V_S = 1.7$ . Density is computed by  $V_P$  via  $1.0 + 1.5 \times (V_P - 1.5)/3.0$ . A single vertical force at (1.75 km, 0.05 km) is used to excite P- and S-waves.

A snapshot of simulated elastic wavefields is shown in Figure 6. Based on the divergence and curl operators, the decomposed scalar and vector potentials are shown in Figure 7. Similar to the previous example, these potential fields do not have correct amplitudes, phases, and units.

In contrast with the Helmholtz decomposition, the separated P- and S-vectors are presented in Figure 8. The Helmholtz decomposition can accurately separate the P- and S-modes and preserve the physical meanings of decomposed wavefields. Figure 9 shows the horizontal and vertical component differences between the input and reconstructed wavefields by summing the P- and S-displacements in Figure 8. Similar to the previous experiment, there are still some numerical artifacts and leakages of shear energies. Overall, their magnitudes are much smaller than the input wavefields.

Once P- and S-waves are accurately separated, I can perform elastic RTM by crosscorrelating the extrapolated source and receiver wavefields. For the Marmousi2 experiment, 128 explosive shots ranging from  $x = 0.2$  to  $x = 3.0$  km and 400 receivers are used. All shots and receivers are located at  $z = 0.05$  km. To reduce the effects of backscattering, the  $V_P$ ,  $V_S$ , and  $\rho$  models are smoothed with a Gaussian operator. A Ricker wavelet with a center frequency of 15 Hz is used in this migration experiment.

If I do not separate the extrapolated source and receiver wavefields, direct component-by-component correlated VV-, VH-, HH-, and HV-images are presented in Figure 10. There are numerous artifacts in

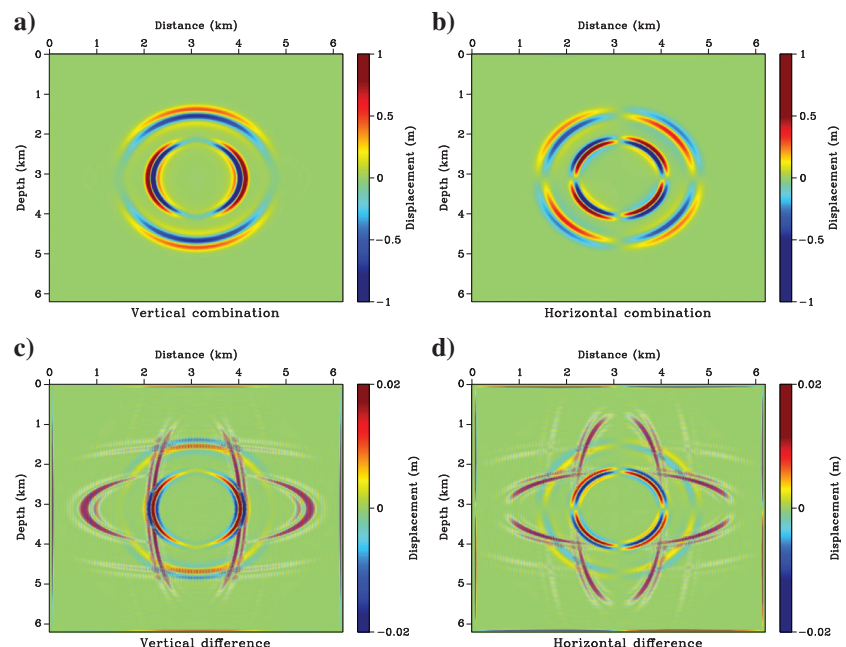


Figure 4. Comparisons between input and reconstructed wavefields. Panels (a and b) are the vertical and horizontal component wavefields by summing isolated P- and S-components in Figure 3. Panels (c and d) are the vertical and horizontal differences between the input and reconstructed wavefields, respectively.

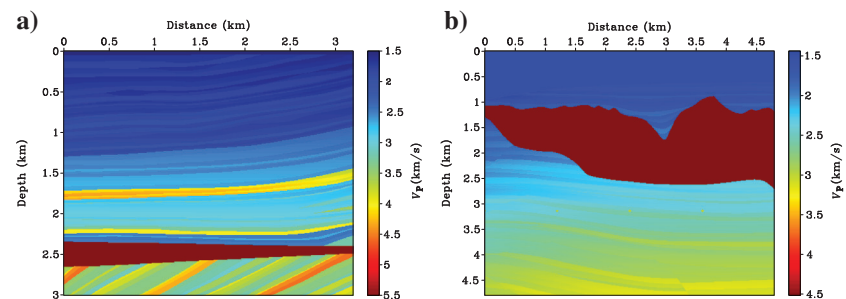


Figure 5. The P-wave velocity models used for the (a) 2D Marmousi2 and (b) Sigsbee experiments.

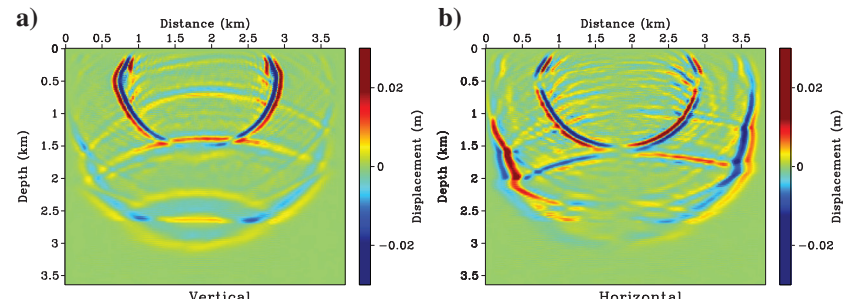


Figure 6. A snapshot of the (a) vertical and (b) horizontal component displacements for the 2D Marmousi2 model. A vertical force at (1.75 km, 0.05 km) is used to excite the P- and S-waves.

these images due to crosstalk between the P- and S-waves. In addition, they do not represent the PP-, PS-, SS-, or SP-reflectivity.

Next, I apply the divergence and curl operators to separate the P- and S-wave modes in the extrapolated wavefields and use a scalar

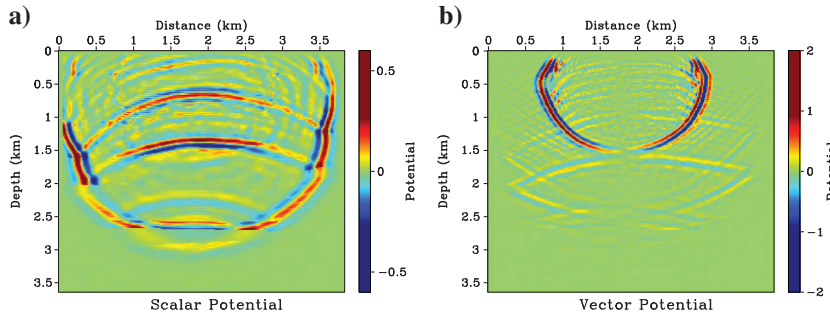


Figure 7. Separated (a) scalar and (b) vector potentials based on the divergence and curl operators for the input wavefields in Figure 6.

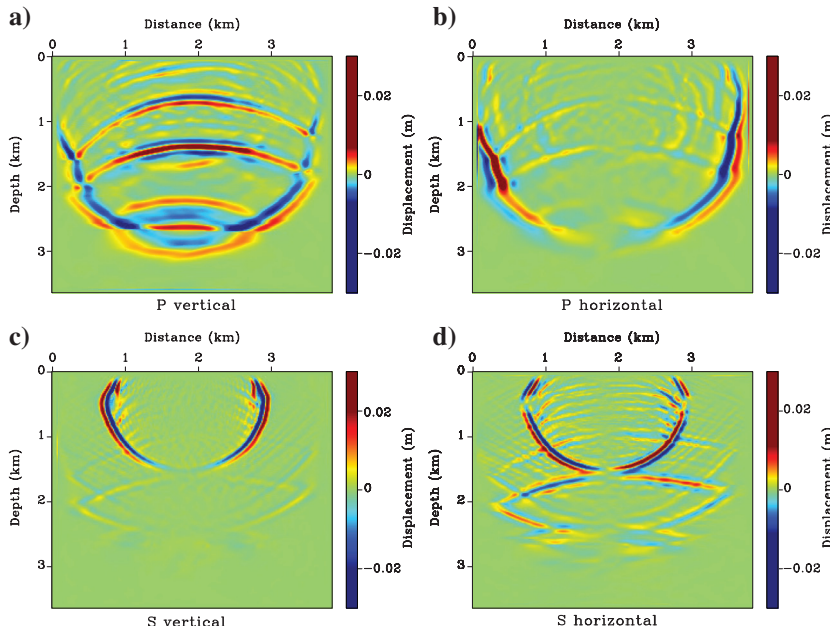


Figure 8. Separated P- and S-wave displacements based on the Helmholtz decomposition for the Marmousi2 experiment. Panels (a) and (b) are the vertical and horizontal component P-wave displacements. Panels (c) and (d) are the vertical and horizontal component S-wave displacements.

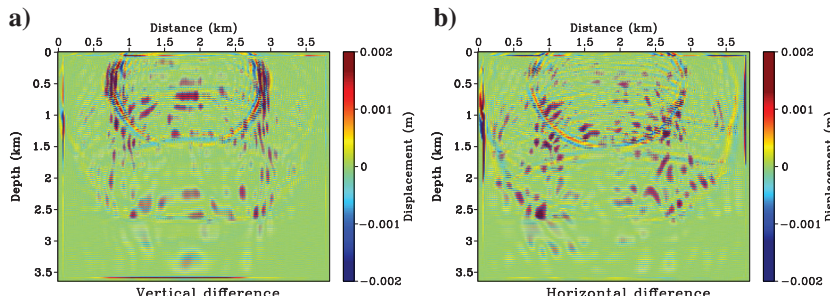


Figure 9. Differences between the input and reconstructed wavefields for the Marmousi2 experiment. Panels (a) and (b) are the vertical and horizontal differences between input wavefields in Figure 6 and reconstructed wavefields by summing P- and S-components in Figure 8.

crosscorrelation imaging condition to construct the PP-, PS-, SS-, and SP-images (Figure 11), although their image qualities are better in comparison with Figure 10. There are no physical meanings for the amplitudes of these results due to amplitude and phase distortions during the wavefield decomposition. In addition, polarity reversals (Du et al., 2012) are observed in the PS- and SP-images.

Next, I present migration images (Figure 12) based on the Helmholtz decomposition (equation 8) and vector imaging conditions (equation 20). Compared with Figure 11, the amplitudes of these images are consistent with the direct component-by-component crosscorrelation results (Figure 10). In addition, the image quality of the new results is much better in comparison with Figures 10 and 11. There are no polarity reversals in these new images due to the correct separation of P-/S-waves and vector imaging conditions.

The previous two examples only involve relatively simple velocity models. To test the performance of this method for models with complicated velocity, I use a portion of the Sigsbee model as the third example (Figure 5b). There is a salt body in the middle of the model, which leads to significant velocity contrasts. The  $V_S$  and density models are calculated from the  $V_P$  model based on the same relations for the Marmousi2 experiment. Figure 13 shows snapshots of the vertical and horizontal component displacements excited by a single force at (2.75 km, 0.05 km). Strong reflections are generated due to the velocity contrast of the salt body.

Figure 14 presents separated scalar and vector potentials based on the divergence and curl operators. Similar to the conclusions for the Marmousi2 experiment, these potentials cannot preserve the amplitudes, phases, and units of the input wavefields.

Figure 15 shows the separated P- and S-displacement vectors based on the Helmholtz decomposition. In addition, Figure 16 compares the vertical and horizontal differences between the input and reconstructed wavefields. Similar to the Marmousi2 experiment, although there are some leakages of shear energies and artifacts in the difference wavefields, the Helmholtz decomposition can accurately separate the P- and S-wave energies for models with large velocity contrasts.

Finally, I compare migration images based on the component-by-component imaging condition, P-/S-wave separation based on the divergence and curl operators, and the Helmholtz decomposition with the vector imaging condition in Figures 17, 18, and 19, respectively. For PS- and SP-images based on the divergence and curl operators, the bottom of the salt body is not very clear. In addition, there are some discontinuities for the top boundary of the salt, which might be

due to the polarity reversal problem. In contrast, PS- and SP-images based on the Helmholtz decomposition and vector imaging condition can better delineate the top and bottom of the salt.

## DISCUSSION

Compared with images based on acoustic approximation, elastic RTM provides us much more information about subsurface. For instance, by simultaneously analyzing PP-, PS-, SS-, and SP-reflections from elastic RTM, we are able to better interpret the physical properties of subsurface materials. However, to correctly image

these reflectivities, we have to accurately separate the P- and S-modes in the extrapolated source and receiver wavefields. As illustrated in the migration images in the previous section, images based on direct component-by-component crosscorrelation suffer from crosstalk between the P- and S-waves. Although the divergence and curl operators have been used in elastic RTM, the decomposed P- and S-waves do not have the correct amplitudes, units, and phases. Therefore, elastic RTM images based on the divergence and curl separations cannot preserve the correct reflectivity information. In addition, there are well-known polarity reversal issues for PS- and SP-images based on the divergence and curl separation.

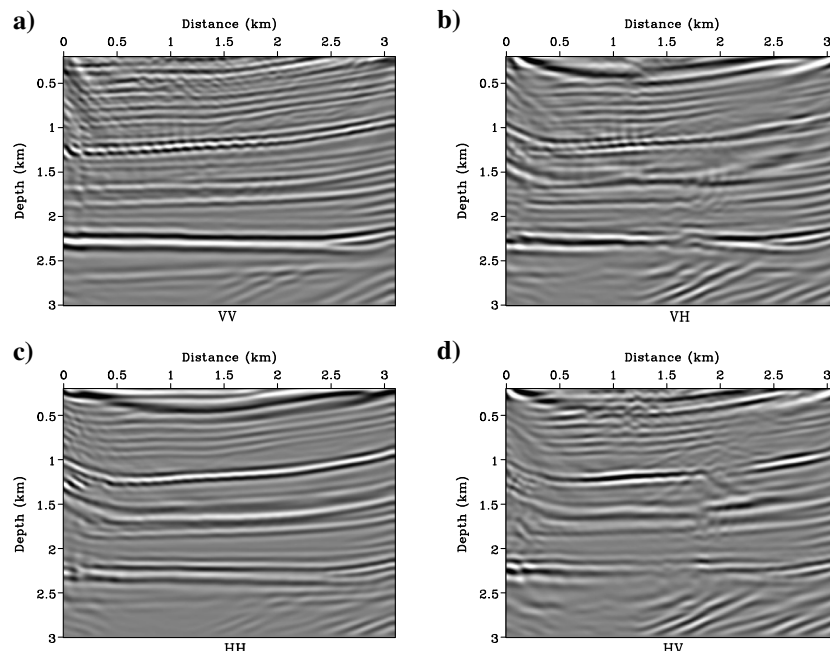


Figure 10. Migrated (a) VV-, (b) VH-, (c) HH-, and (d) HV-images based on the crosscorrelation of the vertical and horizontal component source and receiver wavefields for the Marmousi2 experiment. In this example, 128 explosive shots and 400 receivers are used.

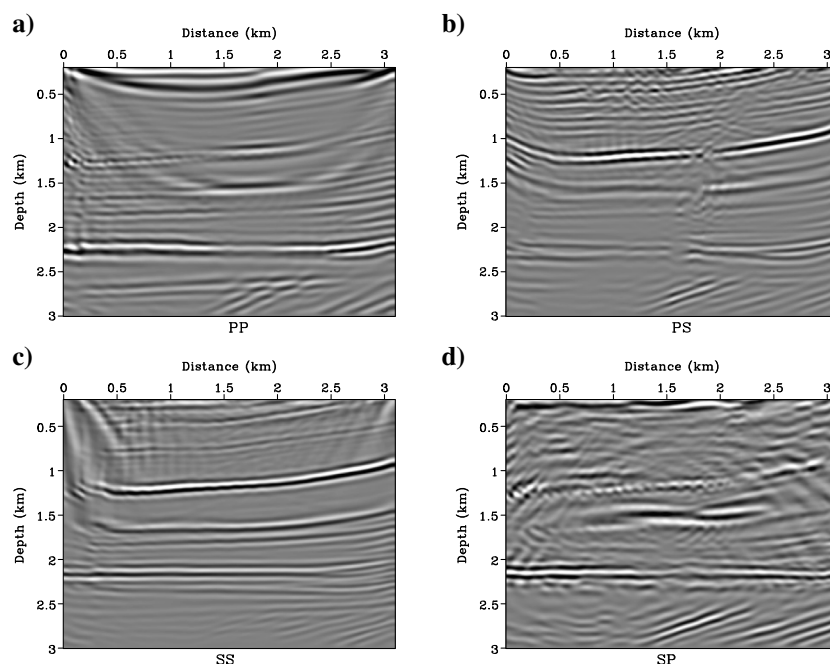


Figure 11. The (a) PP-, (b) PS-, (c) SS-, and (d) SP-images based on separated P-/S-waves with the divergence and curl operators. Polarity reversals are observed in the PS- and SP-images.

To date, several wave-mode decomposition approaches have been proposed to avoid these limitations and accurately separate the P- and S-waves. For instance, Zhang and McMechan (2010) propose a wavenumber method to decompose the P- and S-waves. Ma and Zhu (2003) and Wang and McMechan (2015) introduce an additional stress field during wavefield extrapolation to isolate the P- and S-wave modes. Both methods can accurately decompose the P- and S-vector fields and preserve correct amplitudes, units, and

phases. The development in this paper provides another approach to accurately and efficiently decompose P- and S-waves in elastic media. This approach can be easily extended to 3D cases. Compared with conventional finite difference simulation, we need to add one additional step of P/S decomposition for the wavefields contributed to the crosscorrelation imaging condition. The overall computational costs are relatively small in comparison with finite-difference solvers for elastic-wave equations.

Figure 12. The (a) PP-, (b) PS-, (c) SS-, and (d) SP-images based on separated P/S-waves with the Helmholtz decomposition and vector imaging conditions for the 2D Marmousi2 experiment.

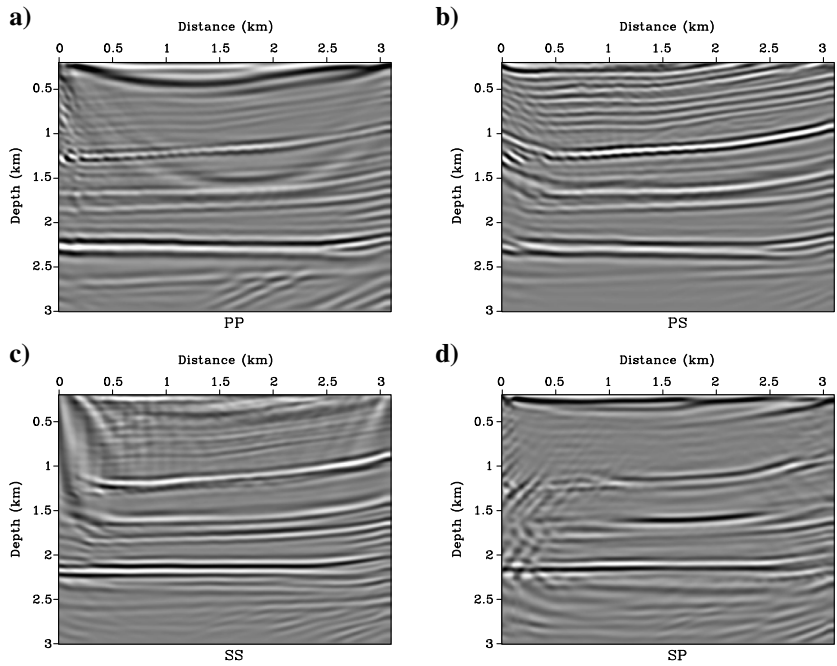


Figure 13. A snapshot of the (a) vertical and (b) horizontal component displacements for the 2D Sigsbee model. A vertical force at (2.75 km, 0.05 km) is used to excite the P- and S-waves.

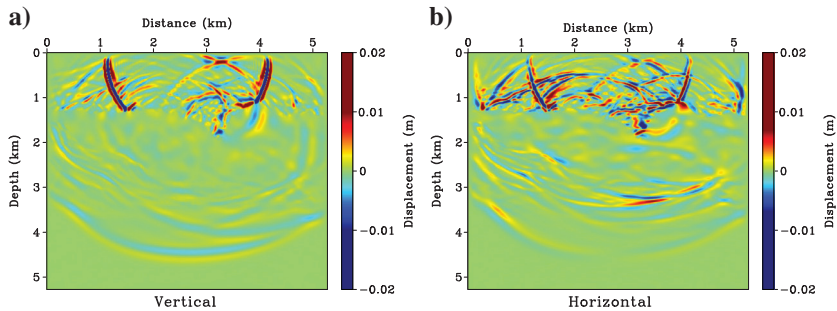
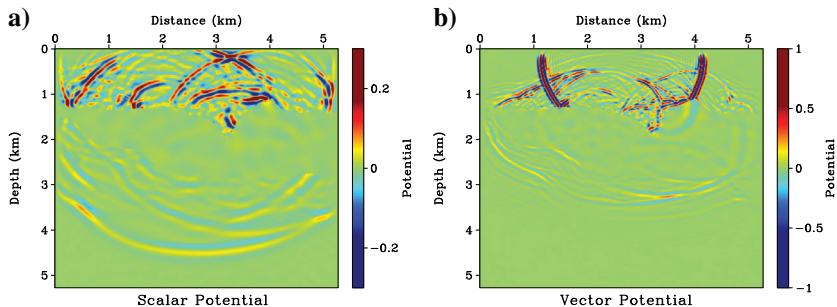


Figure 14. Separated (a) scalar and (b) vector potentials based on the divergence and curl operators for the input wavefields in Figure 13.



## Elastic wavefield separation

S181

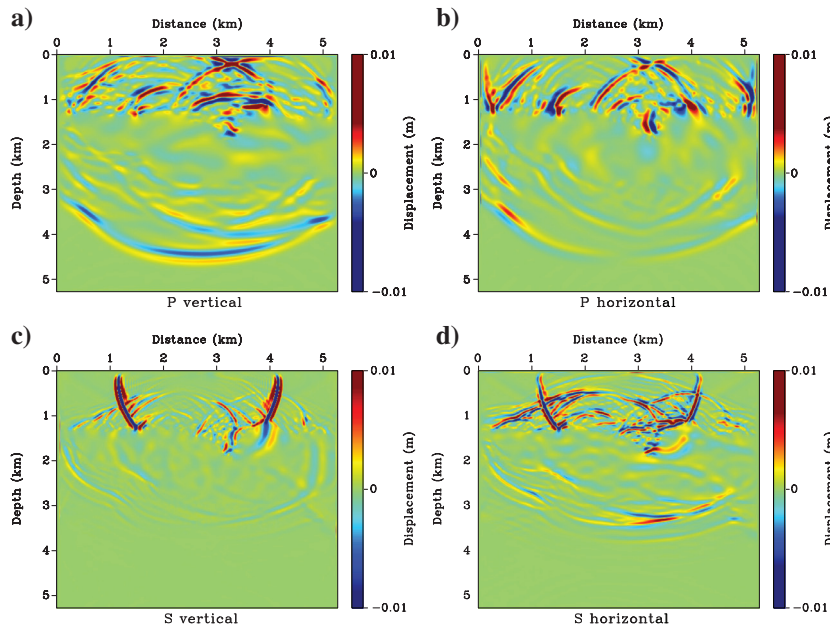


Figure 15. Separated P- and S-wave displacements based on the Helmholtz decomposition for the Sigsbee model. Panels (a) and (b) are the vertical and horizontal component P-waves. Panels (c) and (d) are the vertical and horizontal component S-waves.

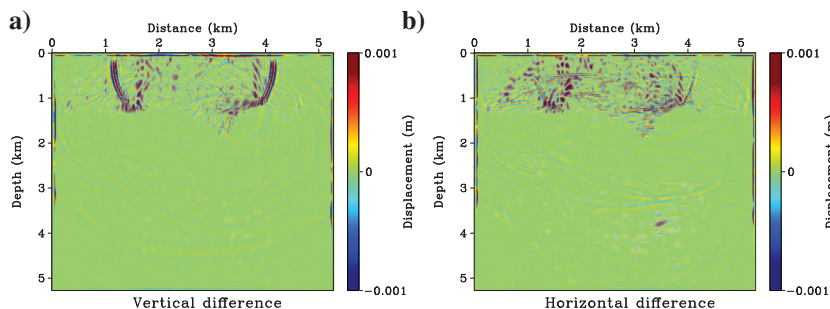


Figure 16. Difference between input and reconstructed wavefields for the Sigsbee model. Panels (a) and (b) are the vertical and horizontal differences between input wavefields in Figure 13 and reconstructed wavefields by summing P- and S-waves in Figure 15.

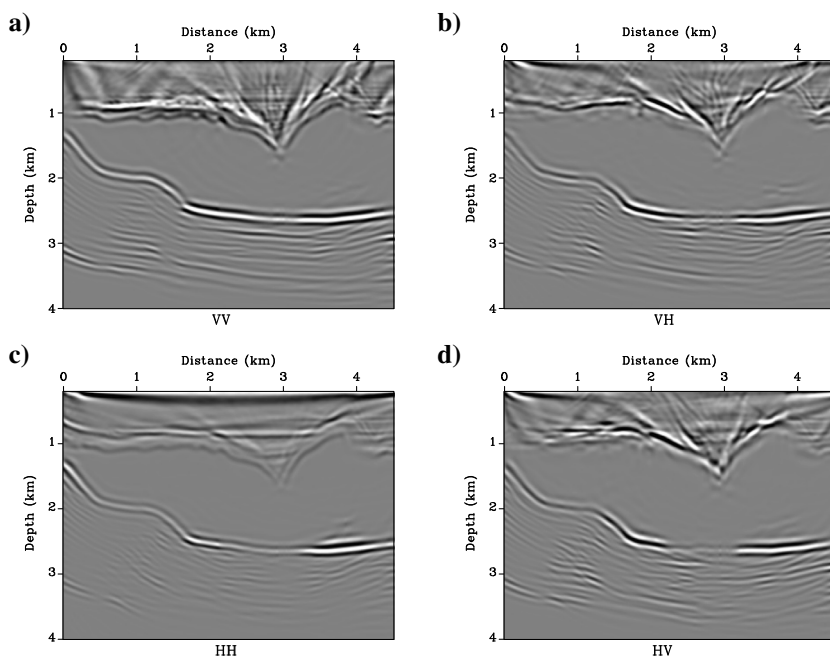


Figure 17. Migrated (a) VV-, (b) VH-, (c) HH-, and (d) HV-images based on the crosscorrelation of the vertical and horizontal component source and receiver wavefields for the 2D Sigsbee experiment. In this example, 128 explosive shots and 400 receivers are used.

Figure 18. The (a) PP-, (b) PS-, (c) SS-, and (d) SP- images based on separated P/S-waves with the divergence and curl operators for the 2D Sigsbee experiment.

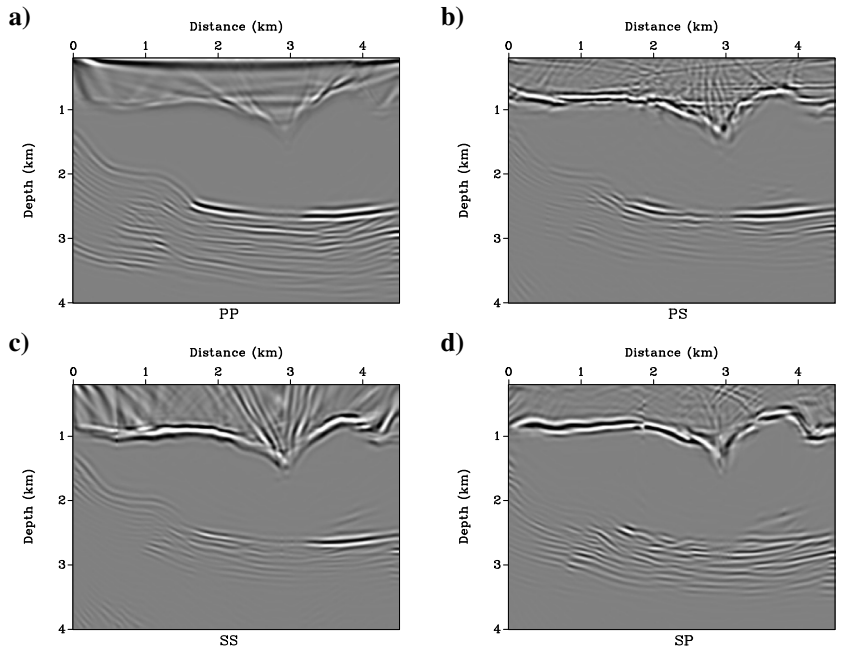
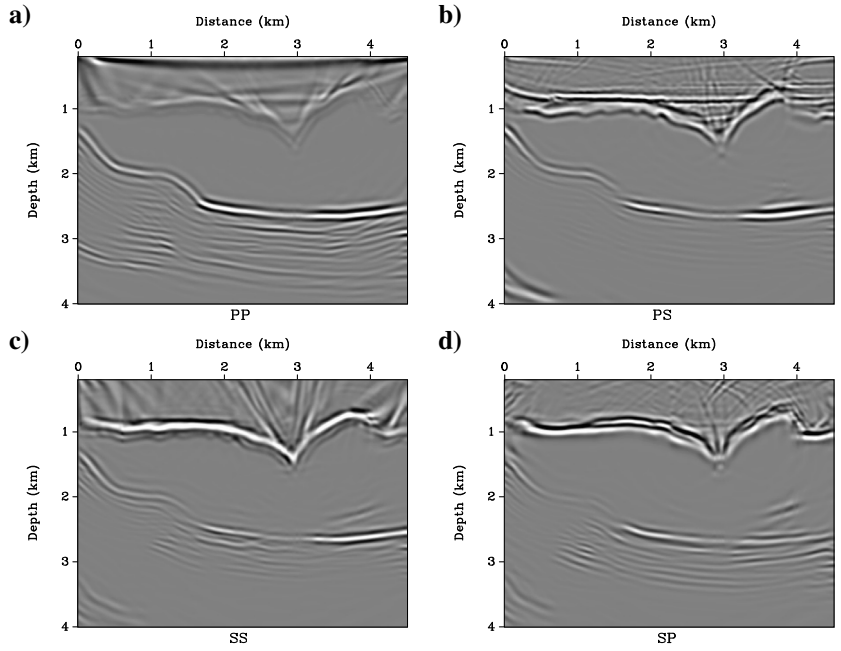


Figure 19. The (a) PP-, (b) PS-, (c) SS-, and (d) SP-images based on separated P/S-waves with the Helmholtz decomposition and vector imaging conditions for the 2D Sigsbee experiment.



## CONCLUSION

In this paper, I propose a new approach to decompose P- and S-waves in extrapolated wavefields based on the application of the Helmholtz decomposition. Instead of directly calculating a multidimensional integral with computational complexity of  $O(N^2)$ , I introduce a new vector field and a vector Poisson's equation. A fast Poisson's solver with computational complexity of  $O(N \log N)$  is used to efficiently solve the vector Poisson's equation. Then, the P- and S-wave modes are isolated based on the differentiations of this new vector field. The decomposed P- and S-waves are vector fields and have the correct amplitudes, units, and phases. The summation

of separated P- and S-waves can accurately reconstruct the extrapolated wavefields. Because the decomposed P- and S-waves are vector fields, vector imaging conditions are used to construct the PP-, PS-, SS-, and SP-images. Elastic RTM results based on this new approach have better image quality and avoid polarity reversal issue in comparison with results based on conventional divergence and curl separation or component-by-component crosscorrelation.

## ACKNOWLEDGMENTS

I thank the Texas Advanced Computing Center for providing computational resources. I appreciate the discussions with G. A.

McMechan about elastic RTM and wavefield decomposition. This paper is contribution no. 1292 from the Department of Geosciences at the University of Texas at Dallas.

## REFERENCES

- Aki, K., and P. Richards, 1980, Quantitative seismology: Theory and methods: W.H. Freeman.
- Baysal, E., D. D. Kosloff, and J. W. Sherwood, 1983, Reverse time migration: *Geophysics*, **48**, 1514–1524, doi: [10.1190/1.1441434](https://doi.org/10.1190/1.1441434).
- Bleistein, N., 1987, On the imaging of reflectors in the earth: *Geophysics*, **52**, 931–942, doi: [10.1190/1.1442363](https://doi.org/10.1190/1.1442363).
- Chang, W., and G. McMechan, 1987, Elastic reverse-time migration: *Geophysics*, **52**, 1365–1375, doi: [10.1190/1.1442249](https://doi.org/10.1190/1.1442249).
- Claerbout, J. F., 1971, Toward a unified theory of reflector mapping: *Geophysics*, **36**, 467–481, doi: [10.1190/1.1440185](https://doi.org/10.1190/1.1440185).
- Douma, H., D. Yingst, I. Vasconcelos, and J. Tromp, 2010, On the connection between artifact filtering in reverse-time migration and adjoint tomography: *Geophysics*, **75**, no. 6, S219–S223, doi: [10.1190/1.3505124](https://doi.org/10.1190/1.3505124).
- Du, Q., Y. Zhu, and J. Ba, 2012, Polarity reversal correction for elastic reverse time migration: *Geophysics*, **77**, no. 2, S31–S41, doi: [10.1190/geo2011-0348.1](https://doi.org/10.1190/geo2011-0348.1).
- Frigo, M., and S. G. Johnson, 2017, FFTW, <http://www.fftw.org>, accessed 6 February 2017.
- Hill, R., 1990, Gaussian beam migration: *Geophysics*, **55**, 1416–1428, doi: [10.1190/1.1442788](https://doi.org/10.1190/1.1442788).
- Hill, R., 2001, Prestack Gaussian-beam depth migration: *Geophysics*, **66**, 1240–1250, doi: [10.1190/1.1487071](https://doi.org/10.1190/1.1487071).
- Liu, F., G. Zhang, S. Morton, and J. Leveille, 2011, An effective imaging condition for reverse-time migration using wavefield decomposition: *Geophysics*, **76**, no. 1, S29–S39, doi: [10.1190/1.3533914](https://doi.org/10.1190/1.3533914).
- Luo, Y., H. Zhu, N. Tarje, M. Christina, and J. Tromp, 2009, Seismic modeling and imaging based upon spectral-element and adjoint methods: *The Leading Edge*, **28**, 568–574, doi: [10.1190/1.3124932](https://doi.org/10.1190/1.3124932).
- Ma, D., and G. Zhu, 2003, P- and S-wave separated elastic wave equation numerical modeling (in Chinese): *Oil Geophysical Prospecting*, **38**, 482–486.
- McMechan, G., 1983, Migration by extrapolation of time-dependent boundary values: *Geophysical Prospecting*, **31**, 413–420, doi: [10.1111/j.1365-2478.1983.tb01060.x](https://doi.org/10.1111/j.1365-2478.1983.tb01060.x).
- Morse, P., and H. Feshbach, 1953, Methods of theoretical physics: McGraw-Hill Book Company.
- Schneider, W., 1978, Integral formulation for migration in two and three dimensions: *Geophysics*, **43**, 49–76, doi: [10.1190/1.1440828](https://doi.org/10.1190/1.1440828).
- Strang, G., 2007, Computational science and engineering: Wellesley-Cambridge Press.
- Sun, R., J. Chow, and K. Chen, 2001, Phase correction in separating P- and S-waves in elastic data: *Geophysics*, **66**, 1515–1518, doi: [10.1190/1.1487097](https://doi.org/10.1190/1.1487097).
- Sun, R., and G. McMechan, 2001, Scalar reverse-time depth migration of prestack elastic seismic data: *Geophysics*, **66**, 1519–1527, doi: [10.1190/1.1487098](https://doi.org/10.1190/1.1487098).
- Sun, R., G. McMechan, C. Lee, J. Chow, and C. Chen, 2006, Prestack scalar reverse-time depth migration of 3D elastic seismic data: *Geophysics*, **71**, no. 5, S199–S207, doi: [10.1190/1.2227519](https://doi.org/10.1190/1.2227519).
- Virieux, J., 1984, SH-wave propagation in heterogeneous media: Velocity-stress finite-difference method: *Geophysics*, **49**, 1933–1942, doi: [10.1190/1.1441605](https://doi.org/10.1190/1.1441605).
- Virieux, J., 1986, P-SV wave propagation in heterogeneous media: Velocity-stress finite-difference method: *Geophysics*, **51**, 889–901, doi: [10.1190/1.1442147](https://doi.org/10.1190/1.1442147).
- Wang, C., J. Cheng, and B. Arntsen, 2016, Scalar and vector imaging based on wave mode decoupling for elastic reverse time migration in isotropic and transversely isotropic media: *Geophysics*, **81**, no. 5, S383–S398, doi: [10.1190/geo2015-0704.1](https://doi.org/10.1190/geo2015-0704.1).
- Wang, W., and G. McMechan, 2015, Vector-based elastic reverse time migration: *Geophysics*, **80**, no. 6, S245–S258, doi: [10.1190/geo2014-0620.1](https://doi.org/10.1190/geo2014-0620.1).
- Whitmore, N., 1983, Iterative depth migration by backward time propagation: 53rd Annual International Meeting, SEG, Expanded Abstracts, 382–385.
- Yan, J., and P. Sava, 2008, Isotropic angle-domain elastic reverse-time migration: *Geophysics*, **73**, no. 6, S229–S239, doi: [10.1190/1.2981241](https://doi.org/10.1190/1.2981241).
- Yan, R., and X. Xie, 2012, An angle-domain imaging condition for elastic reverse time migration and its application to angle gather extraction: *Geophysics*, **77**, no. 5, S105–S115, doi: [10.1190/geo2011-0455.1](https://doi.org/10.1190/geo2011-0455.1).
- Zhang, Q., and G. McMechan, 2010, 2D and 3D elastic wavefield vector decomposition in the wavenumber domain for VTI media: *Geophysics*, **75**, no. 3, D13–D26, doi: [10.1190/1.3431045](https://doi.org/10.1190/1.3431045).
- Zhang, Y., G. Zhang, and N. Bleistein, 2003, True amplitude wave equation migration arising from true amplitude one-way wave equations: *Inverse Problems*, **19**, 1113–1138, doi: [10.1088/0266-5611/19/5/307](https://doi.org/10.1088/0266-5611/19/5/307).
- Zhu, H., Y. Luo, T. Nissen-Meyer, C. Morency, and J. Tromp, 2009, Elastic imaging and time-lapse migration based on adjoint methods: *Geophysics*, **74**, no. 6, WCA167–WCA177, doi: [10.1190/1.3261747](https://doi.org/10.1190/1.3261747).